High-Frequency SiC Three-Phase VSIs With Common-Mode Voltage Reduction and Improved Performance Using Novel Tri-State PWM Method

Junzhong Xu, *Student Member, IEEE*, Jingwen Han, Yong Wang, *Member, IEEE*, Muhammad Ali, and Houjun Tang

***Abstract*—Common-mode voltage (CMV) problem brings severe negative effects in three-phase voltage source inverters (VSIs), particularly for high-frequency silicon (Si) carbide (SiC) VSIs. However, most traditional CMV reduction strategies, which are studied based on Si VSIs, are hard to be implemented and sacrifice the other performance of the VSIs. To overcome such drawbacks, this paper proposes a novel generalized tri-state pulsewidth modulation (GTSPWM) for high-frequency SiC VSIs over power factor of 0–1 and whole linear modulation index range. The working principle of conventional space vector based reduced CMV PWM (RCMV-PWM) methods are reviewed, and their switching signals and CMV patterns are illustrated. The proposed GTSPWM method is described in a generalized scalar PWM approach for simple application and compared with other RCMV-PWM methods. Mathematical analysis, simulations, and experimental results have been used to verify that GTSPWM based high-frequency SiC VSIs can achieve minimum switching losses, improved output waveform quality, smaller dc-link current ripples, and RCMV characteristics. Moreover, with the usage of GTSPWM method, the switching frequency of SiC VSIs can be further increased, and the performance of high-frequency SiC VSIs could be improved appreciably.**

***Index Terms*—Common-mode voltage (CMV), generalized tri-state pulsewidth modulation (GTSPWM), pulsewidth modulation (PWM), silicon carbide (SiC), voltage source inverters (VSIs).**

I. Introduction

WITH THE development of power electronics, three-phase voltage source inverters (VSIs) are widely used in the industry such as AC motor drives, grid-tied photovoltaic systems, and renewable energy conversion. Traditional VSIs based on silicon (Si) devices are undergoing significant changes with the usage of wide band gap semiconductor devices such as Si carbide (SiC), due to their higher switching speed capability, greater thermal conductivity, and increased junction operating temperature. All of these improve the performance of VSIs

Manuscript received December 4, 2017; revised March 1, 2018; accepted April 14, 2018. Date of publication April 23, 2018; date of current version December 7, 2018. This work was supported by the National Natural Science Foundation of China through Project 51577118. Recommended for publication by Associate Editor D. Costinett. *(Corresponding author: Yong Wang.)*

The authors are with the Department of Electrical Engineering, Shanghai Jiao Tong University, Shanghai 200240, China (e-mail:

can reduce the peak-to-peak value of CMV in every switching period and shows a better output performance than other RCMV-PWM methods [16], [17]. However, such method cannot adapt to the change in the load. The second type is carrier-based PWM strategies [18], [19], which utilizes sine PWM (SPWM) with interleaved triangular carriers, and the root mean square (rms) value of CMV is much lower than that in conventional SPWM [18], [19]. But, the peak value of CMV cannot be eliminated completely and the output current ripple is increased. The third type is optimized voltage vectors strategies [20], [21]. The current ripple optimized PWM and the switching loss optimized PWM are proposed in [20]. In [21], optimized nonzero voltage vectors are chose based on the finite-control-set model predictive control methods. However, the calculation of optimization algorithms is complex, which is hard to be implemented practically. In order to reduce the hard-switched losses of three-phase VSIs, different kinds of discontinuous PWM (DPWM) schemes have been proposed [22]–[26]. Conventional DPWM methods such as DPWM0, DPWM1, DPWM2, and DPWM3 are summarized in [22]. To further reduce the switching losses according to the power factor (PF) information, a high performance carrier-based generalized DPWM (GDPWM) method has been well studied in [23], whose modulation wave is phase-shift dependent and captures all of the known discontinuous modulation signals. To meet the applications where unbalanced a three-phase voltage is required to be generated, an extended GDPWM method has been developed in [24]. In [25], a direct digital technique-GDPWM has been presented, which has the advantage of not requiring the load PF information and low computation time. In [26], a novel generalized discontinuous SVPWM (DSVPWMx) is presented by means of local over modulation and linearity transformation. However, all of the aforementioned DPWM methods are focus on the switching losses reduction and pay less attention to the common-mode suppression.

The flexible CMV reduction method with the advantage of low switching losses generated by the modification of modulating or carrier signal is worth of promotion in SiC application. For this purpose, this paper proposes a novel generalized tri-state PWM (GTSPWM) to achieve both CMV reduction and minimum switching losses according to the PF angle for high-frequency SiC three-phase VSIs. Meanwhile, the quality of input and output current waveforms can be improved. The proposed method is feasible over PF of 0–1 and whole linear M_i range. First, the RCMV principles, switching logic signals, and drawbacks in implementation of conventional space vector based RCMV-PWM techniques are reviewed. Thereafter, through a generalized scalar approach [27], GTSPWM is described and illustrated in detail. The phase leg modulation signal for GTSPWM is given and the generation of zero sequence voltage is presented. Then, the performance characteristics, such as switching losses, output current ripples, dc-link current ripples, and common-mode behavior, are investigated and compared via mathematical analysis to show the improved overall performance of GTSPWM. Finally, simulations and experiments are added and discussed to verify the capabilities and excellence of the proposed GTSPWM method. Total harmonic distortion (THD) in current, efficiency, and CMV for various PWM methods are compared by a 5-kW prototype of an SiC-based three-phase VSI in practice.

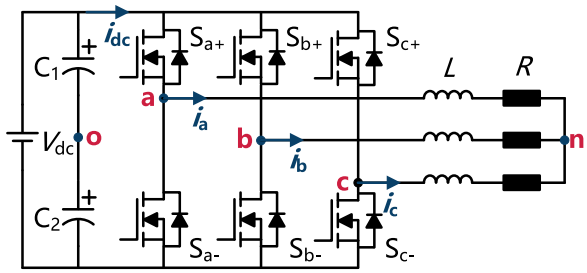

Fig. 1. Three-phase, two-level, and three-wire VSI.

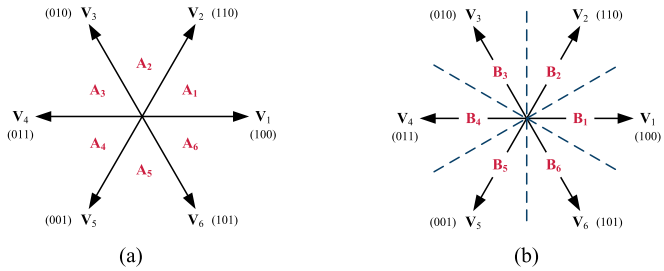

Fig. 2. Voltage space vectors and region definition for space vector based RCMV-PWM methods. (a) Type A regions. (b) Type B regions.

II. Space Vector Based RCMV-PWM Methods

Fig. 1 shows a widely used three-phase-two-level, three-wire SiC VSI with Y-connected *R–L* load. CMV of the inverter is generally defined as the potential difference from the load star point to the neutral point of the dc-bus of the VSI ($V_{\rm no}$ in Fig. 1), and can be expressed as [9]

$$V_{\rm no} = \frac{V_{\rm ao} + V_{\rm bo} + V_{\rm co}}{3} \tag{1}$$

where $V_{\rm ao}$, $V_{\rm bo}$, and $V_{\rm co}$ represent output phase to dc neutral point voltages and take the values of $\pm V_{\rm dc}/2$. With space vector based RCMV-PWM methods, the peak-to-peak value of CMV is successfully reduced from $V_{\rm dc}$ to $V_{\rm dc}/3$ in every switching period T_s.

The selection of active vectors of various space vector based RCMV-PWM methods depends on where reference voltage vector is located. Fig. 2 shows how the vectors divide the space into six segments.

A. Active Zero State Pulsewidth Modulation

The AZSPWM method utilizes the same active vectors to construct the reference voltage vector as the SVPWM. Instead of zero vectors, two opposite active vectors with equal action time are used [9], [13]. The way that active vectors complemented with either group of two near opposing active vectors defines AZSPWM1 and AZSPWM2, while the way that active vectors complemented with one of the active vector and its opposite vector is called AZSPWM3. The simple illustration of AZSPWM1 is given in Fig. 3(a) and AZSPWM3 is given

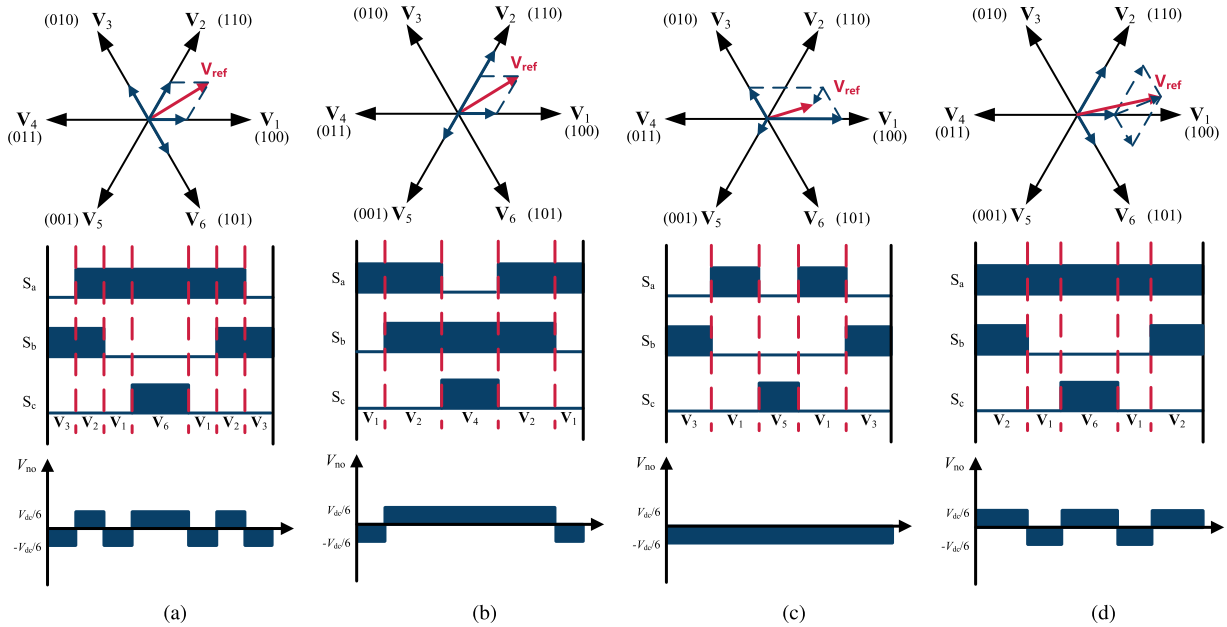

Fig. 3. Illustrations of various space vector based RCMV-PWM methods. (a) AZSPWM1 in region A1. (b) AZSPWM3 in region A1. (C) RSPWM3 in region B1. (d) NSPWM in region B1.

in Fig. 3(b). However, these methods have high output current ripple. Furthermore, the methods except AZSPWM1 will bring about simultaneous commutations in different phase-legs.

B. Remote State Pulsewidth Modulation

The RSPWM method improves the behavior of three-phase inverters in terms of CMV/CMC suppression, via utilizing the active vectors with the same common-mode signature [8]. Three inverter voltage vectors are 120° apart from each other like $\mathbf{V}_1$, $\mathbf{V}_3$, $\mathbf{V}_5$ or $\mathbf{V}_2$, $\mathbf{V}_4$, $\mathbf{V}_6$. RSPWM1 utilizes only one vector group and apply the vectors in a fixed sequence. RSPWM2 uses one group as well, but a variable sequence is selected to improves the waveform quality. RSPWM3 utilizes both vector groups and alternates each group every 60° to extend the voltage linearity region. The simplified illustration of RSPWM3 is given in Fig. 3(c). Practically, the application of RSPWM methods is restricted because of low voltage utilization and simultaneous phase-leg switching behavior.

C. Near-State Pulsewidth Modulation

The NSPWM method [14] utilizes a group of three active voltage vectors to synthesize the desired reference voltage. These three active vectors are selected such that the inverter voltage vector closest to reference voltage vector and its two neighbors are utilized. A simplified illustration of NSPWM is given in Fig. 3(d). The main drawback of NSPWM is its limited linearity range ($0.61 \leq M_i \leq 0.906$).

D. Tri-State Pulsewidth Modulation

The TSPWM method [16], [17] utilizes three selected voltage vectors to construct the reference voltage vector [16]. The utilized voltage vectors are altered every 60° throughout the space.

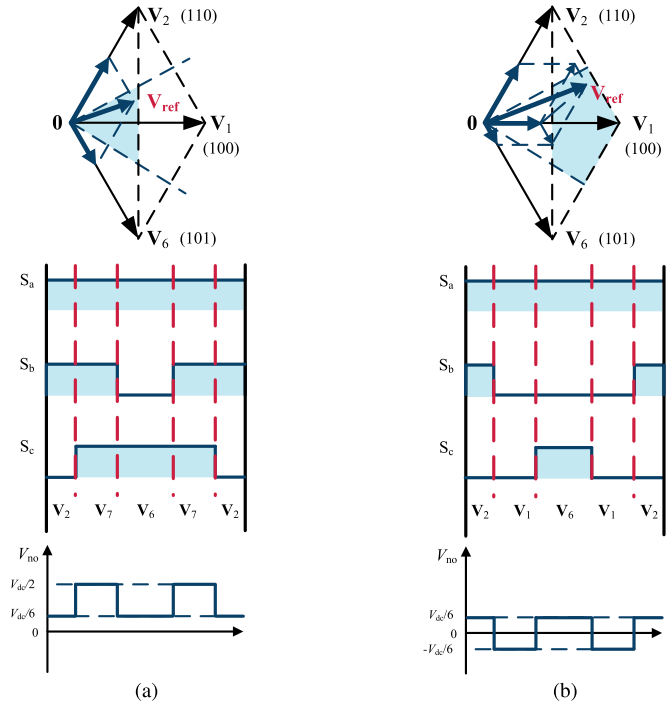

Fig. 4. Illustrations of TSPWM. (a) T region. (b) P region.

Taking region B1 as an example, if reference voltage vector $\mathbf{V}_{\text{ref}}$ is located in the triangular region (T region), as shown in Fig. 4(a), two active space vectors with a difference of 120°, $\mathbf{V}_2$ and $\mathbf{V}_6$, are selected to generate the required output voltages. One zero vector, $\mathbf{V}_7$ is applied, to compensate the remaining time in one switching period and also to achieve minimum switching action. Meanwhile, with the selected zero vector ap-

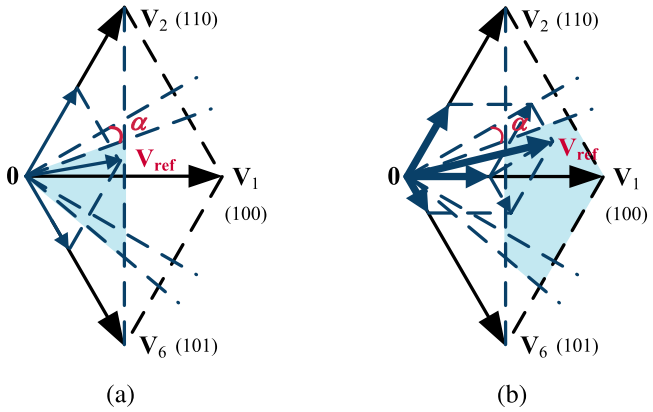

Fig. 5. Vector synthesis for GTSPWM method. (a) T region. (b) P region.

plied in each sector, the peak-to-peak value of the CMV can be reduced to $V_{\rm dc}/3$ in every switching period T_s. $\mathbf{V}_{\rm ref}$ in T region can be expressed as

$$\begin{cases} \mathbf{V}_{\rm ref}T_s = \mathbf{V}_2T_2 + \mathbf{V}_6T_6 \\ T_s = T_2 + T_6 + T_7. \end{cases} \tag{2}$$

If the $\mathbf{V}_{\rm ref}$ is located in the pentagonal region (P region), as shown in Fig. 4(b), three active voltage vectors, such as $\mathbf{V}_1$, $\mathbf{V}_6$, and $\mathbf{V}_2$, are utilized. Since nonzero vectors are used, CMV is successfully reduced to $\pm V_{\rm dc}/6$. If the value of M_i is between 0.61 and 0.907, TSPWM operated in this region is the same as NSPWM. The reference voltage vector in the P region is expressed by

$$\begin{cases} \mathbf{V}_{\rm ref}T_s = \mathbf{V}_2T_2 + \mathbf{V}_6T_6 + \mathbf{V}_1T_1 \\ T_s = T_2 + T_6 + T_1. \end{cases} \tag{3}$$

III. Implementation of the Proposed Method

After the recognition of similarities and relationships between TSPWM and NSPWM, a generalized TSPWM method is proposed to get both CMV reduction and minimum switching losses under different loads. In aid of illustrating the GTSPWM, PF angle φ and modulator phase angle α are introduced, where $\alpha = \frac{\pi}{6}$ at $\varphi > \frac{\pi}{6}$, $\alpha = -\frac{\pi}{6}$ at $\varphi < -\frac{\pi}{6}$, and $\alpha = \varphi$ elsewhere. The region definition of GTSPWM is rotated by α as shown in Fig. 5. The duty cycle of each phase leg in region B1 can be derived from (2) and (3), and stated as

$$\begin{cases} d_a = 1 \\ d_b = 1 - \dfrac{2\sqrt{3}}{\pi} M_i \cos\left(\omega t + \dfrac{\pi}{6}\right) \\ d_c = 1 + \dfrac{2\sqrt{3}}{\pi} M_i \cos\left(\omega t + \dfrac{5\pi}{6}\right). \end{cases} \tag{4}$$

Modulation signals for GTSPWM can be easily calculated in (5) [22], and the result for phase leg a is summarized in Table I

$$V_x^{**} = \frac{1}{2}V_{\rm dc} \cdot (2d_x - 1) \qquad x \in \{a, b, c\}. \tag{5}$$

For simple practical application, GTSPWM can be simply implemented through generalized scalar PWM approach [27].

TABLE I
Phase Leg Modulation Signal for GTSPWM

60° Sextant	Phase Leg a ($\frac{V_{\rm a}^{**}}{V_{\rm dc}/2}$)
$-\frac{\pi}{6} - \alpha \le \omega t \le \frac{\pi}{6} - \alpha$	1
$\frac{\pi}{6} - \alpha \le \omega t \le \frac{\pi}{2} - \alpha$	$-1 - \frac{4\sqrt{3}}{\pi} M_i \cos(\omega t + \frac{5\pi}{6})$
$\frac{\pi}{2} - \alpha \le \omega t \le \frac{5\pi}{6} - \alpha$	$1 + \frac{4\sqrt{3}}{\pi} M_i \cos(\omega t + \frac{\pi}{6})$
$\frac{5\pi}{6} - \alpha \le \omega t \le \pi - \alpha$	-1
$-\pi - \alpha \le \omega t \le -\frac{5\pi}{6} - \alpha$	-1
$-\frac{5\pi}{6} - \alpha \le \omega t \le -\frac{\pi}{2} - \alpha$	$1 - \frac{4\sqrt{3}}{\pi} M_i \cos(\omega t + \frac{5\pi}{6})$
$-\frac{\pi}{2} - \alpha \le \omega t \le -\frac{\pi}{6} - \alpha$	$-1 + \frac{4\sqrt{3}}{\pi} M_i \cos(\omega t + \frac{\pi}{6})$

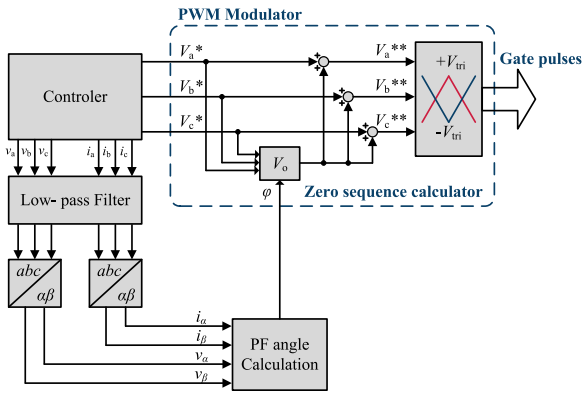

Fig. 6. Control block diagram of proposed GTSPWM method with zero-sequence signal injection and two phase-opposed triangular carriers.

Modulation waveforms $V_{\rm a}^{**}$, $V_{\rm b}^{**}$, and $V_{\rm c}^{**}$ of GTSPWM are represented as

$$\begin{cases} V_{\rm a}^{**} = V_{\rm a}^{*} + V_0 = V_{1\rm m}\cos(\omega t) + V_0 \\ V_{\rm b}^{**} = V_{\rm b}^{*} + V_0 = V_{1\rm m}\cos(\omega t - 2\pi/3) + V_0 \\ V_{\rm c}^{**} = V_{\rm c}^{*} + V_0 = V_{1\rm m}\cos(\omega t + 2\pi/3) + V_0 \end{cases} \tag{6}$$

where V_0 is the zero sequence voltage and $\omega t = \theta$ represents the angle of the reference voltage vector.

Instead of the single polarity carrier wave as GDPWM in [23], two phase-opposed triangular carriers $+V_{\rm tri}$ and $-V_{\rm tri}$ are utilized to produce gate pulses of the inverters as shown in Fig. 6. The three-phase voltages (v_a, v_b, and v_c) and three-phase currents (i_a, i_b, and i_c) are sampled and converted to v_α, v_β and i_α, i_β (conversion of $a-b-c$ frame to $\alpha-\beta$ frame). Upon that, PF angle φ is acquired as

$$|\varphi| = \arccos\left(\frac{v_\alpha i_\alpha + v_\beta i_\beta}{\sqrt{v_\alpha^2 + v_\beta^2} \cdot \sqrt{i_\alpha^2 + i_\beta^2}}\right) \tag{7}$$

$$\varphi = \begin{cases} |\varphi| & \arctan\dfrac{v_\beta}{v_\alpha} \ge \arctan\dfrac{i_\beta}{i_\alpha} \\ -|\varphi| & \arctan\dfrac{v_\beta}{v_\alpha} < \arctan\dfrac{i_\beta}{i_\alpha}. \end{cases} \tag{8}$$

The polarity of triangular carrier to be compared with the modulation signals is sector dependent to obtain CMV suppres-

TABLE II
CHOICE OF SECTOR-DEPENDENT CARRIER WAVE

	B_1	B_2	B_3	B_4	B_5	B_6
Phase a	V_{tri}	$-V_{tri}$	$-V_{tri}$	V_{tri}	V_{tri}	V_{tri}
Phase b	V_{tri}	V_{tri}	V_{tri}	$-V_{tri}$	$-V_{tri}$	V_{tri}
Phase c	$-V_{tri}$	V_{tri}	V_{tri}	V_{tri}	V_{tri}	$-V_{tri}$

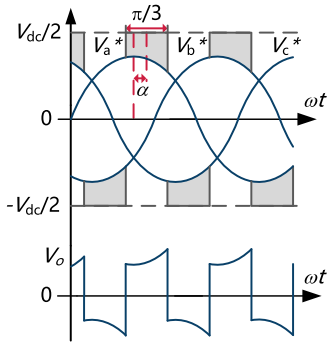

Fig. 7. GTSPWM zero-sequence signal generation method.

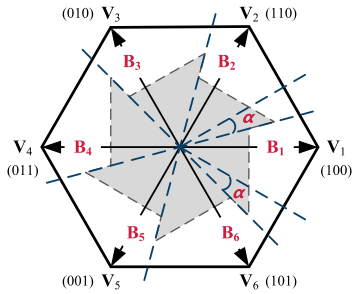

Fig. 8. Voltage vector plane of the proposed GTSPWM strategy.

sion, as given in Table II. The zero-sequence signal generation method of GTSPWM is illustrated in Fig. 7. Via adjusting the clamped phase of modulation waves, GTSPWM realizes the minimum switching losses action under different loads as well. All three reference modulation signals $V_{\rm a}^*$, $V_{\rm b}^*$, and $V_{\rm c}^*$ are phase shifted by α. Thus, the three new signals are obtained: $V_{{\rm a}\alpha}^*$, $V_{{\rm b}\alpha}^*$, and $V_{{\rm c}\alpha}^*$ as in (9), which determine the zero sequence signal in (10), where the one with maximum magnitude among $V_{{\rm a}\alpha}^*$, $V_{{\rm b}\alpha}^*$, and $V_{{\rm c}\alpha}^*$ is first defined as $V_{x\alpha}^*$ and V_x^*

$$\begin{cases} V_{{\rm a}\alpha}^* = V_{1{\rm m}}\cos(\omega t-\alpha) \\ V_{{\rm b}\alpha}^* = V_{1{\rm m}}\cos(\omega t-2\pi/3-\alpha) \\ V_{{\rm c}\alpha}^* = V_{1{\rm m}}\cos(\omega t+2\pi/3-\alpha) \end{cases} \tag{9}$$

$$V_0 = {\rm sign}(V_{x\alpha}^*)\cdot V_{\rm dc}/2 - V_x^* \qquad x\in\{a,b,c\}. \tag{10}$$

Furthermore, to keep the modulator linear, the region of utilized space sectors should be rotated by α. A new allocation of voltage vector plane for GTSPWM is shown in Fig. 8, which is quite different from GDPWM and other RCMV-PWM methods. When taking the scalar PWM approach, GTSPWM method is easy to implement in digital signal processing (DSP) with enhanced pulsewidth modulator units.

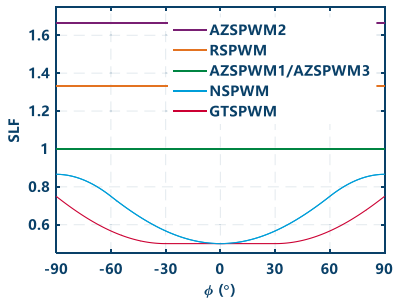

Fig. 9. SLF characteristics of various RCMV-PWM methods.

IV. PERFORMANCE COMPARISON OF SPACE VECTOR BASED RCMV-PWM METHODS

Increasing the switching frequency of the SiC VSIs, many merits of GTSPWM in comparison with the other space vector based RCMV-PWM methods are quite obvious, which are discussed as follows.

A. Switching Losses

The switching losses of a VSI is dependent on load-current, which varies with the PWM method employed. Assuming a linear dependence of per switching losses, the average value of per device switching loss over a fundamental cycle $P_{\rm sw}$ can be derived as follows [22], [23]:

$$P_{\rm sw} = \frac{V_{\rm dc}f_{\rm s}(t_{\rm on}+t_{\rm off})}{4\pi}\int_0^{2\pi} i_{\rm sa}(\omega t)\,{\rm d}\omega t. \tag{11}$$

In (11), $t_{\rm on}$ and $t_{\rm off}$ can be approximately regarded as turn-on and turn-off time of the devices, and $f_{\rm s}$ represents the switching frequency of the devices. $i_{\rm sa}(\omega t)=0$ when the switching state of corresponding phase is clamped at "$+V_{\rm dc}/2$" or "$-V_{\rm dc}/2$" and $i_{\rm sa}=|i_{\rm a}(\omega t)|$otherwise. $P_{\rm sw}$ is normalized to $P_{\rm sw\_0}$ in (12), which is based on the switching losses of the Si VSI using continuous PWM methods such as SPWM and SVPWM under based frequency $f_{\rm s\_0}$. The switching loss function (SLF) of GTSPWM can be derived as shown in (13) and (14), where $K_{\rm f}=f_{\rm s\_0}/f_{\rm s}$, and $K_{\rm s}$ is a coefficient whose value is relevant to the materials of switching device. Since hard-switch losses in SiC devices are reduced by at least 50% compared to conventional Si devices under the same $f_{\rm s}$ [6], $K_{\rm s}=1$ for Si devices and 2 for SiC devices

$$P_{\rm sw\_0} = \frac{V_{\rm dc}I_{\rm max}f_{\rm s\_0}}{\pi}\times(t_{\rm on\_Si}+t_{\rm off\_Si}) \tag{12}$$

$${\rm SLF}_{\rm GTPWM} = \frac{P_{\rm sw\_GTSPWM}}{P_{\rm sw\_0}} \tag{13}$$

$$= \begin{cases} \dfrac{1}{2K_{\rm s}K_{\rm f}} & |\varphi|\le\dfrac{\pi}{6} \\ \dfrac{2+\sin\left(|\varphi|-\dfrac{2\pi}{3}\right)}{2K_{\rm f}K_{\rm s}} & \dfrac{\pi}{6}\le|\varphi|\le\dfrac{\pi}{2}. \end{cases} \tag{14}$$

SLF characteristics of various RCMV-PWM methods with unit $K_{\rm s}$ and $K_{\rm f}$ are compared in Fig. 9. In this case, switching losses of GTSPWM are minimum for any φ among various

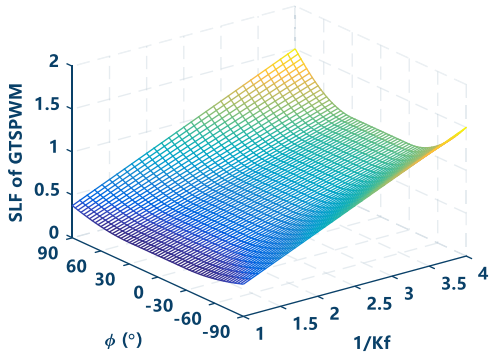

Fig. 10. SLF characteristics of GTSPWM when $K_{\rm s} = 2$.

TABLE III
NUMBER OF COMMUTATIONS PER-CYCLE AND THE CHOICE OF K_f

	Number of Commutations	K_f
SVPWM	6	1
DPWM1	4	2/3
AZSPWM1	6	1
AZSPWM2	10	5/3
AZSPWM3	6	1
RSPWM	8	4/3
NSPWM	4	2/3
GTSPWM	4	2/3

RCMV-PWM methods, which leads to a reduced heat sink size and higher power density of the inverter. With the application of SiC devices, SLF of GTSPWM-based inverters for different $K_{\rm f}$ and α are shown in Fig. 10. On the premise of equivalent switching losses, the switching frequency can be adapted to improve the output current quality following (15). Within $-30^\circ \le \varphi \le 30^\circ$, switching frequency of GTSPWM-based SiC inverter can be increased by at least four times relative to traditional continuous PWM methods based Si inverter

$$K_{\rm f} = \begin{cases} \dfrac{1}{4} & |\varphi| \le \dfrac{\pi}{6} \\ \dfrac{2 + \sin\left(|\varphi| - \dfrac{2\pi}{3}\right)}{4} & \dfrac{\pi}{6} \le |\varphi| \le \dfrac{\pi}{2}. \end{cases} \tag{15}$$

B. Output Current Ripple

The performance of the inverter output current ripple can be studied theoretically through harmonic flux trajectories [13], [22]. With the aid of space vectors, an intuitive approach to analyze the switching frequency harmonic characteristics of the inverter output voltage vector is well investigated, and the conceptual harmonic flux $\lambda_{\rm h}$ is defined to evaluate the performance of output current ripple. The normalized harmonic flux vector $\lambda_{\rm hn}$ investigated in terms of the time integral of the harmonic voltage vector in a PWM cycle is shown as follows:

$$\lambda_{\rm hn}(M_i, \theta, V_{\rm dc}) = \frac{\pi}{V_{\rm dc} T_{\rm s}} \int_0^{T_{\rm s}} (\mathbf{V}_k - \mathbf{V}_{\rm ref}) {\rm d}t \qquad k \in \{0, 1, 2 \ldots 7\}. \tag{16}$$

Since different space vector based RCMV-PWM methods differ in the construction of the voltage vectors, the harmonic flux trajectories of each PWM modulator are various. RMS harmonic flux $\lambda_{\rm hn-rms}$ over a PWM cycle is given in (17), where d is the duty cycle. Taking the number of commutations per cycle into account, the square-rms harmonic flux is scaled with $K_{\rm f}^2$ for fair comparison. $K_{\rm f}$ for each PWM method using the same devices is given in Table III, where GTSPWM takes 2/3 as a default value. The calculation of normalized harmonic distortion factor (HDF) over a fundamental cycle is shown in (18)

$$\lambda_{\rm hn-rms}(M_i, \theta) = \sqrt{\int_0^1 \lambda_{\rm hn}^2 {\rm d}d} \tag{17}$$

$${\rm HDF} = f(M_i) = K_{\rm f}^2 \times \frac{288}{2\pi^3} \int_0^{2\pi} \lambda_{\rm hn-rms}^2 {\rm d}d. \tag{18}$$

The resulting HDF functions of the discussed space vector based RCMV-PWM methods are given as follows:

$${\rm HDF}_{\rm AZSPWM1} = \left(\frac{432}{\pi^4} - \frac{324\sqrt{3}}{\pi^5}\right) M_i^4 - \frac{96\sqrt{3}}{\pi^4} M_i^3 + \left(\frac{72\sqrt{3}}{\pi^3} - \frac{72}{\pi^2}\right) M_i^2 + \frac{8}{3} \tag{19}$$

$${\rm HDF}_{\rm AZSPWM2} = \left(\frac{1200}{\pi^4} - \frac{900\sqrt{3}}{\pi^5}\right) M_i^4 + \frac{800\sqrt{3}}{\pi^4} M_i^3 + \left(\frac{200}{3\pi^2} - \frac{600\sqrt{3}}{\pi^3}\right) M_i^2 + \frac{200}{27} \tag{20}$$

$${\rm HDF}_{\rm AZSPWM3} = \left(\frac{432}{\pi^4} - \frac{324\sqrt{3}}{\pi^5}\right) M_i^4 - \frac{48}{\pi^2} M_i^2 + \frac{8}{3} \tag{21}$$

$${\rm HDF}_{\rm RSPWM1} = \frac{512}{\pi^4} M_i^4 - \frac{256}{9\pi^2} M_i^2 + \frac{256}{81} \tag{22}$$

$${\rm HDF}_{\rm RSPWM2} = \left(\frac{512}{\pi^4} - \frac{64\sqrt{3}}{\pi^5}\right) M_i^4 + \frac{256\sqrt{3}}{\pi^4} M_i^3 - \frac{256}{9\pi^2} M_i^2 - \frac{256}{9\sqrt{3}\pi^2} M_i + \frac{256}{81} \tag{23}$$

$${\rm HDF}_{\rm RSPWM3} = \left(\frac{512}{\pi^4} - \frac{384\sqrt{3}}{\pi^5}\right) M_i^4 + \frac{512}{3\pi^4} M_i^3 - \frac{256}{9\pi^2} M_i^2 - \frac{512}{27\pi^2} M_i + \frac{256}{81} \tag{24}$$

$$\mathrm{HDF_{NSPWM}} = \left(\frac{384}{\pi^4} + \frac{96\sqrt{3}}{\pi^5}\right) M_i^4 - \frac{128}{\pi^4} M_i^3 - \left(\frac{64}{\pi^2} - \frac{128\sqrt{3}}{\pi^3}\right) M_i^2 + \frac{128}{\pi^2} M_i - \frac{64}{27}. \quad (25)$$

The HDF function of the GTSPWM method for any value of α is composed of multiple segments. Considering B1 region as an example, for $0 \le M_i \le 0.52$, all reference vectors are located in the T region and $\lambda_{\mathrm{hn-rms}}$ is derived linearly with the space vectors $\mathbf{V}_2$, $\mathbf{V}_6$, and $\mathbf{V}_7$. In this case, HDF function under unit PF is given in (26). For $\frac{\pi}{6\cos(\frac{\pi}{6}+|\alpha|)} \le M_i \le 0.906$, reference vectors are located in the P region instead, and $\lambda_{\mathrm{hn-rms}}$ can be derived linearly with $\mathbf{V}_2$, $\mathbf{V}_6$, and $\mathbf{V}_1$. In this case, HDF function under unit PF is the same as that of NSPWM in (25). In the range of $0.52 \le M_i \le \frac{\pi}{6\cos(\frac{\pi}{6}+|\alpha|)}$, the region (T region or P region) of the reference vector should be determined first and can be expressed as in (27) and (28), where λ_{rms1} is the $\lambda_{\mathrm{hn-rms}}$ calculated in the T region, λ_{rms2} is the $\lambda_{\mathrm{hn-rms}}$ calculated in the P region, and $\beta = \gamma = \arccos\frac{\pi}{6M_i}$

$$\mathrm{HDF_{GTSPWM-low}} = \left(\frac{96\sqrt{3}}{\pi^5} + \frac{384}{\pi^4}\right) M_i^4 - \frac{1536M_i^3}{\pi^4} + \left(\frac{64\sqrt{3}}{\pi^3} + \frac{64}{\pi^2}\right) M_i^2 \quad (26)$$

$$\mathrm{HDF_{GTSPWM-mid}} = K_\mathrm{f}^2 \times \frac{3\times 288}{\pi^3} h \quad (27)$$

$$h = \begin{cases} \int_{-\frac{\pi}{6}-\alpha}^{-\beta} \lambda_{\mathrm{rms1}}^2 \mathrm{d}d + \int_{-\beta}^{\beta} \lambda_{\mathrm{rms2}}^2 \mathrm{d}d + \int_{\beta}^{\frac{\pi}{6}-\alpha} \lambda_{\mathrm{rms1}}^2 \mathrm{d}d \\ \qquad 0.52 \le M_i \le \frac{\pi}{6\cos(\frac{\pi}{6}-|\alpha|)} \\ \int_{-\frac{\pi}{6}-\alpha}^{-\gamma} \lambda_{\mathrm{rms1}}^2 \mathrm{d}d + \int_{-\gamma}^{\frac{\pi}{6}-\alpha} \lambda_{\mathrm{rms2}}^2 \mathrm{d}d \\ \qquad 0 \le \alpha \le \frac{\pi}{6}, \frac{\pi}{6\cos(\frac{\pi}{6}-|\alpha|)} \le M_i \le \frac{\pi}{6\cos(\frac{\pi}{6}+|\alpha|)} \\ \int_{-\frac{\pi}{6}-\alpha}^{\gamma} \lambda_{\mathrm{rms2}}^2 \mathrm{d}d + \int_{\gamma}^{\frac{\pi}{6}-\alpha} \lambda_{\mathrm{rms1}}^2 \mathrm{d}d \\ \qquad \frac{-\pi}{6} \le \alpha < 0, \frac{\pi}{6\cos(\frac{\pi}{6}-|\alpha|)} \le M_i \le \frac{\pi}{6\cos(\frac{\pi}{6}+|\alpha|)}. \end{cases} \quad (28)$$

With the HDF function, the output current ripple characteristics of different methods can be calculated, which is dependent on M_i. HDF characteristic of GTSPWM for different M_i and α is shown in Fig. 11. The HDF characteristics of GTSPWM under unit PF (the worst case of GTSPWM) and other RCMV-PWM methods are compared in Fig. 12(a). It can be seen that GSTPWM is excelling to all other RCMV-PWM methods. HDF comparison of GTSPWM and conventional PWM methods, SVPWM and DPWM1, is shown in Fig. 12(b). Reducing K_f means increasing the switching frequency that leads to smaller HDF. According to (15), on the premise of equivalent switching losses, K_f can take 1/4 in SiC VSIs within $-30° \le \varphi \le 30°$. In this case, the performance of GTSPWM is better than that of SVPWM operating under the based frequency. Based on the comparisons in Fig. 12, an optimal switching frequency for SiC VSIs when using GTSPWM can be chosen and a compromise between switching losses and output harmonics will be made.

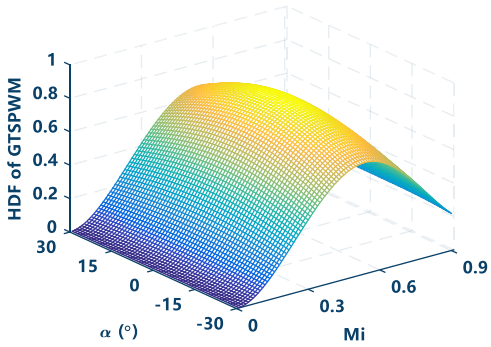

Fig. 11. HDF characteristic of GTSPWM.

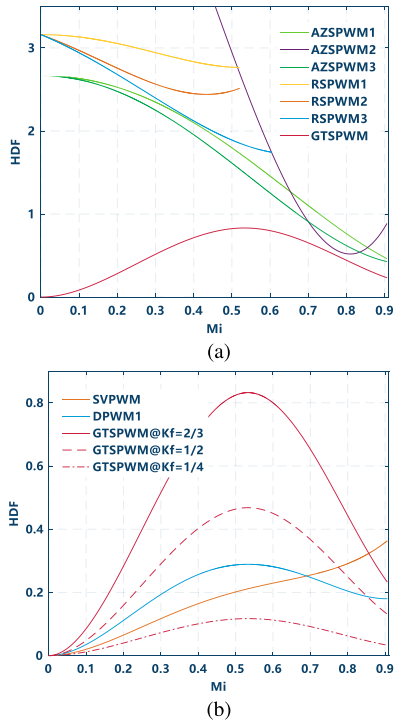

Fig. 12. HDF comparison between various PWM methods. (a) GTSPWM and other RCMV-PWM methods. (b) GTSPWM with various K_f and conventional PWM methods.

Reduced HDF leads to lower ripple with the same filter size or smaller output filter size for the same current ripple value. HDF of GTSPWM is lower than that of other RCMV-PWM methods, but it is still higher than conventional SVPWM and DPWM methods. However, such shortcoming can be overcome with the increased f_s in SiC inverters. Therefore, GTSPWM based high-frequency SiC inverters have the performance of RCMV and lesser output current ripple simultaneously.

C. DC-Link Current Ripple

The harmonic current rms value I_{inhrms} of the inverters input side is important for dc-bus capacitor size design, which is used

to absorb the PWM ripple current [8], [13]. The dc-link current ripple of each RCMV-PWM method is various and is a function of M_i and φ. To compare the dc-link current ripple characteristic of the RCMV-PWM methods, the dc-link current ripple factor $K_{\rm dc}$ is defined as following [22], [28]:

$$I_{\rm inhrms}^2 = I_{\rm rms}^2 - I_{\rm avg}^2 \tag{29}$$

$$K_{\rm dc} = \frac{I_{\rm inhrms}^2}{I_{\rm 1rms}^2} \tag{30}$$

where $I_{\rm 1rms}$ is the rms value of ac output fundamental component current, $I_{\rm rms}$ is the rms value of the inverter input current, and $I_{\rm avg}$ is the mean value of the inverter input current, respectively.

For a given PWM method, $I_{\rm inhrms}$ can be derived over a fundamental cycle [29], and (30) can be calculated analytically. The $K_{\rm dc}$ factor for SVPWM and discussed RCMV-PWM methods are summarized as follows [13]:

$$K_{\rm dc}^{\rm SVPWM} = -\frac{18}{\pi^2}M_i^2\cos^2\varphi + \left(\frac{2\sqrt{3}}{\pi^2} + \frac{8\sqrt{3}}{\pi^2}\cos^2\varphi\right)M_i \tag{31}$$

$$K_{\rm dc}^{\rm AZSPWM1-2} = -\frac{18}{\pi^2}M_i^2\cos^2\varphi + \frac{9\sqrt{3}}{\pi^2}M_i\cos 2\varphi + 1 - \frac{3\sqrt{3}}{2\pi}\cos 2\varphi \tag{32}$$

$$K_{\rm dc}^{\rm AZSPWM3} = \left(\frac{3\sqrt{3}}{2\pi^2}\cos 2\varphi - \frac{15}{2\pi^2}\sin 2\varphi\right)M_i + 1 + \frac{3\sqrt{3}}{4\pi}\cos 2\varphi + \frac{9}{4\pi}\sin 2\varphi \tag{33}$$

$$K_{\rm dc}^{\rm RSPWM} = -\frac{18}{\pi^2}M_i^2\cos^2\varphi + \frac{6}{\pi^2}M_i\cos 2\varphi + 1 \tag{34}$$

$$K_{\rm dc}^{\rm NSPWM} = -\frac{18}{\pi^2}M_i^2\cos^2\varphi + \frac{24}{\pi^2}M_i\cos 2\varphi + 1 - \frac{3\sqrt{3}}{\pi}\cos 2\varphi. \tag{35}$$

$K_{\rm dc}$ of GTSPWM for $0 \le M_i \le 0.52$ is shown in (36). For $\frac{\pi}{6\cos(\frac{\pi}{6}+|\alpha|)} \le M_i \le 0.906$, $K_{\rm dc}$ of GTSPWM is displayed in (37). In the range of $0.52 \le M_i \le \frac{\pi}{6\cos(\frac{\pi}{6}+|\alpha|)}$, the calculation of $I_{\rm rms}$ in this case is segmented and is given in (38), where $I_{\rm rms1}$ is the $I_{\rm rms}$ calculated in the T region, and $I_{\rm rms2}$ is the $I_{\rm rms}$ calculated in the P region

$$K_{\rm dc}^{\rm GTSPWM-low} = \begin{cases} -\frac{18M_i^2\cos^2\varphi}{\pi^2} + \frac{12M_i\cos\varphi}{\pi^2} & |\varphi| \le \frac{\pi}{6} \\ -\frac{18M_i^2\cos^2\varphi}{\pi^2} - \left(\frac{6\sin 2|\varphi|}{\pi^2} + \frac{9\sqrt{3}}{\pi^2}\right)M_i & |\varphi| > \frac{\pi}{6} \end{cases} \tag{36}$$

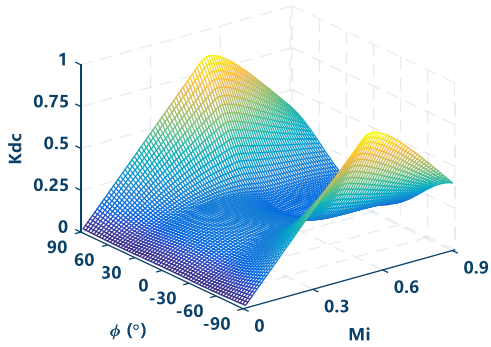

Fig. 13. $K_{\rm dc}$ characteristic of GTSPWM.

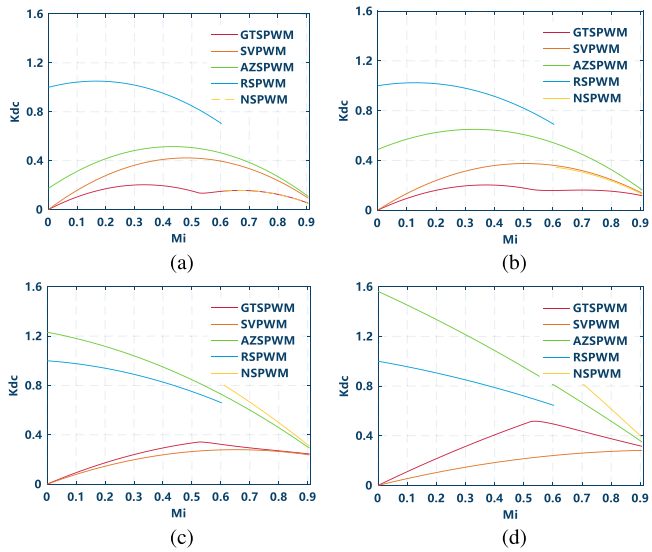

Fig. 14. $K_{\rm dc}$ for various PWM methods. (a) PF = 1. (b) PF = 0.9. (c) PF = 0.6. (d) PF = 0.4.

$$K_{\rm dc}^{\rm GTSPWM-high} = -\frac{18M_i^2\cos^2\varphi}{\pi^2} + \frac{24M_i\cos\varphi}{\pi^2} - \frac{3\sqrt{3}}{\pi} + 1 \quad |\varphi| \le \arccos\frac{\sqrt{3}}{3} - \frac{\pi}{6} \tag{37}$$

$$I_{\rm rmsmid}^2 = \begin{cases} \int_{-\frac{\pi}{6}-\varphi}^{-\beta} I_{\rm rms1}^2\,{\rm d}d + \int_{-\beta}^{\beta} I_{\rm rms2}^2\,{\rm d}d + \int_{\beta}^{\frac{\pi}{6}-\varphi} I_{\rm rms1}^2\,{\rm d}d \\ \qquad |\varphi| \le \frac{\pi}{6}, 0.52 \le M_i \le \frac{\pi}{6\cos(\frac{\pi}{6}-|\alpha|)} \\ \int_{-\frac{\pi}{6}-\alpha}^{-\gamma} I_{\rm rms1}^2\,{\rm d}d + \int_{-\gamma}^{\frac{\pi}{6}-\alpha} I_{\rm rms2}^2\,{\rm d}d \\ \qquad \varphi > 0, \frac{\pi}{6\cos(\frac{\pi}{6}-|\alpha|)} \le M_i \le \frac{\pi}{6\cos(\frac{\pi}{6}+|\alpha|)} \\ \int_{-\frac{\pi}{6}-\alpha}^{\gamma} I_{\rm rms2}^2\,{\rm d}d + \int_{\gamma}^{\frac{\pi}{6}-\alpha} I_{\rm rms1}^2\,{\rm d}d \\ \qquad \varphi < 0, \frac{\pi}{6\cos(\frac{\pi}{6}-|\alpha|)} \le M_i \le \frac{\pi}{6\cos(\frac{\pi}{6}+|\alpha|)}. \end{cases} \tag{38}$$

$K_{\rm dc}$ characteristic of GTSPWM for different M_i and φ is shown in Fig. 13. Comparison of various RCMV-PWM methods under different PF is shown in Fig. 14. For a high PF as shown in Fig. 14(a) and (b), common condition in practice, $K_{\rm dc}$ of

GTSPWM is lower than all other RCMV-PWM methods. For a low PF shown in Fig. 14(c) and (d), $K_{\rm dc}$ of GTSPWM is inferior to conventional SVPWM method, but it is still superior to other RCMV-PWM methods. Therefore, GTSPWM-based high-frequency SiC inverters have the advantage of reduced dc-link current as well, which decreases the size of dc-bus capacitor and further improve the power density of the SiC inverters.

D. Common-Mode Behavior

The CMV characteristics influence the inverter performance significantly, because high-frequency behavior results in unavoidable CMC. To determine the influence of CMV on CMC, a double Fourier integral analysis is applied to calculate the harmonic components of CMV for different RCMV-PWM methods [30]. In general terms, the harmonic component of the switching phase leg output voltage under given carrier index variable m (of the switching frequency f_s) and fundamental index variable n (of the modulating frequency f_o) is given in (39). The CMV of inverters can be expressed as (40), where $y_s(i)$, $y_e(i)$, $x_r(i)$, and $x_f(i)$ are the outer and inner double Fourier integral limits, which are determined by PWM method. $\omega_s = 2\pi f_s$ is the carrier angular frequency, and $\omega_o = 2\pi f_o$ is the fundamental angular frequency

$$C_{\rm mn} = \frac{1}{2\pi^2}\sum_{i=0}^{6}\int_{y_s(i)}^{y_e(i)}\int_{x_r(i)}^{x_f(i)} 2V_{\rm dc}e^{j(mx+ny)}{\rm d}x{\rm d}y \quad (39)$$

$$V_{\rm no} = \sum_{m=1}^{\infty}\sum_{n=-\infty}^{\infty} C_{\rm mn}\cdot\cos(m\omega_s t + n\omega_o t)$$
$$n = 3p, p = 0, 1, 2\ldots \quad (40)$$

Solutions of (39) for SVPWM and DPWM1 can be found in [30], and that of AZSPWM1 and GTSPWM are developed as in (41) and (42) shown at the bottom of next page. Since the resonant frequency of the common-model equivalent circuit is close to the PWM frequency [10], the harmonic component of CMV for the first $f_{\rm s}$ is the most dominant in generating CMC.

Maximum harmonic component of CMV around the first $f_{\rm s}$ of GTSPWM for different M_i and α is shown in Fig. 15(a). Fig. 15(b) shows the maximum harmonic component of CMV around the first $f_{\rm s}$, where $m = 1$, $n = 0$ for SVPWM and DPWM1, and $m = 1$, $n = 3$ for AZPWM1 and GTSPWM. As illustrated in Fig. 15(b), GTSPWM and AZPWM1 have advantage over SVPWM and DPWM1. For low M_i, harmonic component of GTSPWM is lower than all other PWM techniques. So it confirms the effectiveness of GTSPWM in reducing CMV.

V. Simulation Results

In order to verify the analytical results, PLECS-based simulation model has been developed. The circuit used in the simulation is the same as the one given in Fig. 1. Three-phase Y-connected *R–L* load is used, where R = 10 Ω and L = 10 mH. The frequency of output voltage is 50 Hz. The dc-link voltage is chosen to be 700 V. The dc-link capacitance is 470 μF. On the premise of equivalent switching count, the switching frequency

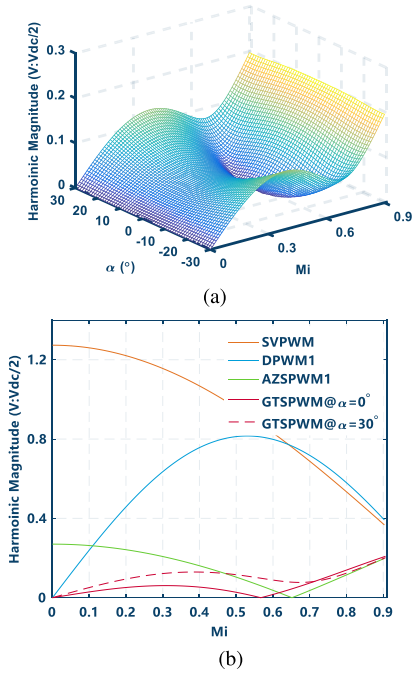

Fig. 15. Maximum harmonic of CMV around the first $f_{\rm s}$. (a) GTSPWM with regard to M_i and α. (b) Comparison with PWM methods.

of each considered RCMV-PWM method is adjusted, where $f_s^{\rm AZSPWM1} = f_s^{\rm AZSPWM3} = 20$ kHz, $f_s^{\rm AZSPWM2} = 12$ kHz, $f_s^{\rm RSPWM3} = 15$ kHz, and $f_s^{\rm NSPWM} = f_s^{\rm GTSPWM} = 30$ kHz.

Simulation waveforms of output phase current, modulation signal, and CMV for GTSPWM are shown in Fig. 16. Since φ is less than 30°, the switching device that conducts the largest current is held on, which reduces the switching losses by at least 50% compared to continuous SVPWM methods. In Fig. 17, with the output frequency increased from 20 to 80 Hz, PF angle of the load φ is changed from 7.16° to 26.69°, which can be achieved through (7) and (8) and added into zero sequence voltage calculation. The RCMV performance and least switching losses characteristics of GTSPWM are still satisfied.

The comparison of output phase current simulation waveforms is overlaid in Fig. 18. The advantage of GTSPWM is remarkable for $M_i = 0.2$, and it is still superior to other RCMV-PWM methods when $M_i = 0.8$. The current ripple of GTSPWM at $M_i = 0.8$ is slightly better than that of NSPWM as expected.

Fig. 19 shows the dc-link current waveforms for various PWM methods. For $M_i = 0.2$, the rms values are 4.60, 7.86, 6.31, and 1.24 A for AZSPWM1/2, AZSPWM3, RSPWM3, and GTSPWM, respectively. These are 28.03, 30.18, 26.76, and 26.35 A for AZSPWM1/2, AZSPWM3, NSPWM, and GTSPWM, when $M_i = 0.8$. GTSPWM is superior for these cases as predicted with the $K_{\rm dc}$ curve in Fig. 14.

Fig. 20 shows the frequency spectrum analysis of the CMV for various RCMV-PWM methods. The value of harmonic magnitude is normalized to $V_{\rm dc}/2$. To improve the accuracy of Fourier analysis, switching frequency is set to be 10 kHz. For $M_i = 0.2$, although GTSPWM has large harmonic in the low frequency, the first harmonic is least among all other RCMV-PWM

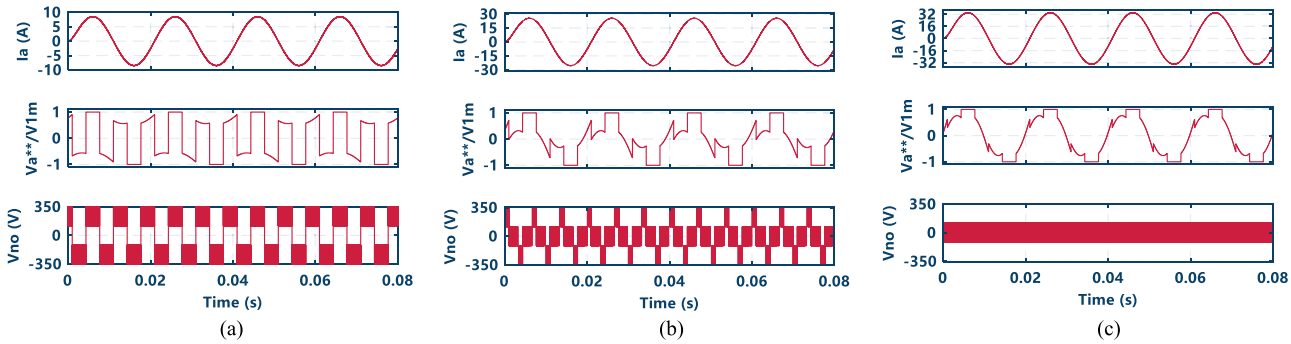

Fig. 16. Simulation waveforms for GTSPWM. (a) $M_i = 0.2$. (b) $M_i = 0.6$. (c) $M_i = 0.8$.

methods. For $M_i = 0.8$, the first harmonic magnitude of GTSPWM is still better than that of AZSPWM2 and AZSPWM3.

VI. Experimental Verification

A 5-kW prototype of an SiC three-phase inverter has been fabricated to verify the proposed GTSPWM method in practice and compare with other PWM methods. An open-loop test is conducted with different PWM methods generated by a TMS320F28335 DSP control board, as shown in Fig. 21. Specific parameters of the prototype are listed in Table IV. Since AZSPWM2, AZSPWM3, and RSPWM have simultaneous inverter-leg switchings performance, which restricts their practical application, only AZSPWM3 is implemented as a representative of this group. NSPWM method is not considered in the experiment because the PF angle of the experiment is small and the performance of NSPWM is similar with GTSPWM. On the premise of equivalent switching count, f_s for SVPWM, AZSPWM1, and AZSPWM3 is set as 40 kHz, while that for DPWM1 and GTSPWM is 60 kHz.

Fig. 22 shows the experimental waveforms of the gate signal, output current, and the CMV under different M_i for the proposed GTSPWM method. Fig. 22(a) shows the results under $M_i = 0.2$,

$$
\begin{aligned}
C_{\mathrm{mn}}^{\mathrm{AZSPWM1}} = \frac{8U_{\mathrm{dc}}}{m\pi^2}\Bigg\{ & \tfrac{1}{jn}\sin\tfrac{m\pi}{2}(1+2\cos\tfrac{n\pi}{3})\sin^2\tfrac{n\pi}{6}[J_0(3mM_i)+2\cos\tfrac{n\pi}{3}J_0(\sqrt{3}mM_i)] \\
& +\tfrac{\pi}{6}\sin\tfrac{n\pi}{2}\cos\tfrac{m\pi}{2}[2\cos\tfrac{n\pi}{6}J_n(\sqrt{3}mM_i)+J_n(3mM_i)] \\
& +\sum_{\substack{k=1\\(2k+1\neq n)}}^{\infty}\tfrac{1}{n-2k-1}\sin\tfrac{(m+2k+1)\pi}{2}\sin\tfrac{(n-2k-1)\pi}{6}\cos\tfrac{(n-2k-1)\pi}{2} \\
& \times[2\cos\tfrac{(2n-6k-3)\pi}{6}J_k(\sqrt{3}mM_i)+J_k(3mM_i)] \\
& +\sum_{\substack{k=1\\(2k\neq n)}}^{\infty}\tfrac{1}{j(n-2k)}\sin\tfrac{(m+2k)\pi}{2}\sin\tfrac{(n-2k)\pi}{6}\sin\tfrac{(n-2k)\pi}{2} \\
& \times[2\cos\tfrac{(n-3k)\pi}{3}J_k(\sqrt{3}mM_i)+J_k(3mM_i)] \\
& +\sum_{\substack{k=1\\(2k+1\neq -n)}}^{\infty}\tfrac{1}{n+2k+1}\sin\tfrac{(m+2k+1)\pi}{2}\sin\tfrac{(n+2k+1)\pi}{6}\cos\tfrac{(n+2k+1)\pi}{2} \\
& \times[2\cos\tfrac{(2n+6k+3)\pi}{6}J_k(\sqrt{3}mM_i)+J_k(3mM_i)] \\
& +\sum_{\substack{k=1\\(2k\neq -n)}}^{\infty}\tfrac{1}{j(n+2k)}\sin\tfrac{(m+2k)\pi}{2}\sin\tfrac{(n+2k)\pi}{6}\sin\tfrac{(n+2k)\pi}{2} \\
& \times[2\cos\tfrac{(n+3k)\pi}{3}J_k(\sqrt{3}mM_i)+J_k(3mM_i)]
\end{aligned}
\Bigg\} \tag{41}
$$

$$
\begin{aligned}
C_{\mathrm{mn}}^{\mathrm{GTSPWM}} = \frac{2U_{\mathrm{dc}}}{m\pi^2}\Bigg\{ & \sum_{\substack{k=1\\(k\neq -n)}}^{\infty}\tfrac{1}{j(n+k)}\sin\tfrac{k\pi}{2}J_k(2\sqrt{3}mM_i)[1+\cos(n+k)\pi] \\
& \times[e^{j\frac{(n-k)\pi}{3}}-\cos m\pi][e^{j[\frac{(-3n+2k)\pi}{6}-\alpha(n+k)]}-e^{j[\frac{-5n\pi}{6}-\alpha(n+k)]}] \\
& +\sum_{\substack{k=1\\(k\neq n)}}^{\infty}\tfrac{1}{j(n-k)}\sin\tfrac{k\pi}{2}J_k(2\sqrt{3}mM_i)[1+\cos(n-k)\pi] \\
& \times[e^{j\frac{(n+k)\pi}{3}}-\cos m\pi][e^{j[\frac{(-3n-2k)\pi}{6}-\alpha(n-k)]}-e^{j[\frac{-5n\pi}{6}-\alpha(n-k)]}] \\
& +\tfrac{2\pi}{3}\sin\tfrac{n\pi}{2}J_n(2\sqrt{3}mM_i)[e^{-j\frac{n\pi}{6}}-\cos(m\pi)e^{-j\frac{5n\pi}{6}}]
\end{aligned}
\Bigg\}. \tag{42}
$$

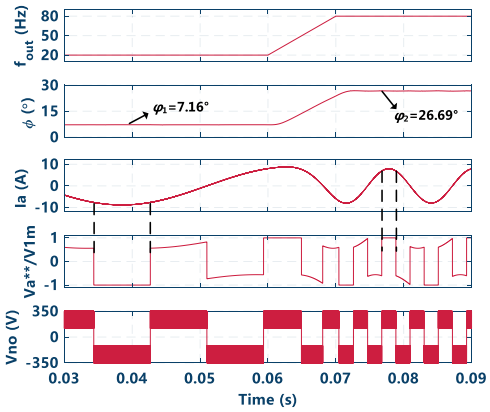

Fig. 17. Simulation waveforms for GTSPWM at $M_i = 0.2$ when the PF of the load is varying.

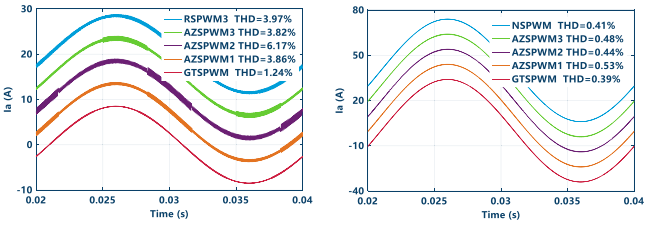

Fig. 18. Simulation current comparison. (a) $M_i = 0.2$. (b) $M_i = 0.8$.

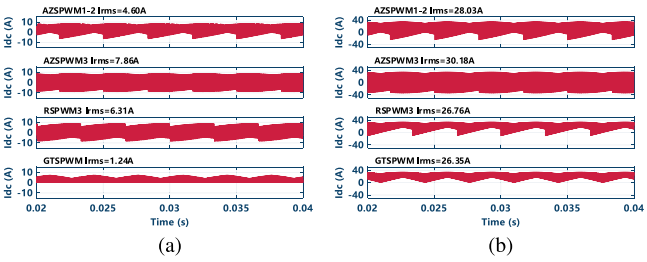

Fig. 19. DC-link current waveforms for various RCMV-PWM method. (a) $M_i = 0.2$. (b) $M_i = 0.8$.

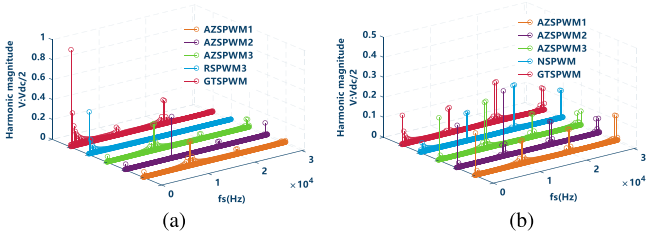

Fig. 20. Frequency spectrum of CMV for various RCMV-PWM methods. (a) $M_i = 0.2$. (b) $M_i = 0.8$.

and the reference vector is in the T region. Fig. 22(c) shows the results under $M_i = 0.8$, and the reference vector is in the P region. The CMV in the transition between T region and P region is shown in Fig. 22(b). In the P region, the peak-peak value of CMV is restricted to $V_{\rm dc}/3$, while in the T region and transition

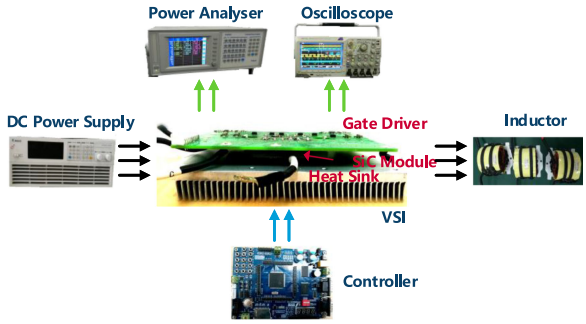

Fig. 21. Prototype of 5-kW SiC VSI and experimental setup for the open-loop test.

TABLE IV
SPECIFICATIONS OF SiC VSI

Parameter	Value
DC-link voltage	700 V
DC capacitor	470 μF
Output frequency	50 Hz
Switching frequency	20 k - 100 kHz
Load resistor	54 Ω
Load inductor	0.95 mH
SiC module	*10-PZ126PA080MR-M909F28Y*

region, it is reduced to $V_{\rm dc}/3$ in each sector and every PWM cycle, as discussed in Sections II and III. From Fig. 22(a) and (b), although the CMV wave has a large low-frequency signal, it has minor effect on generating CMC. Meanwhile, it can be found that there are no unexpected CMV peaks in GTSPWM due to deadtime effect. Therefore, the proposed GTSPWM method is effective in reducing the CMV.

Experiment current waveforms of output phase current for GTSPWM, AZSPWM1, and AZSPWM3 are overlaid in Fig. 23. The current ripple of GTSPWM is better than others as expected. Due to the influence of nonidealities such as deadtime effect, minimum pulsewidth restrictions, and parasitic impedance in the experiment, there is a high spike in output current at low M_i. The comparison results of current THD for GTSPWM and other PWM methods are shown in Fig. 24. Current THD of GTSPWM is superior to RCMV-PWM methods especially at low M_i, as seen in Fig. 24(a). But it is inferior to SVPWM, on the premise of equivalent switching count. With the switching frequency increased in high-frequency SiC inverters, such shortcoming can be overcome, as shown in Fig. 24(b).

The current ripple of the dc-link is reduced for the GTSPWM as compared to AZSPWM1, AZSPWM3, DPWM1, and SVPWM, as observed from Fig. 25. The dc-link current ripple is reduced from 2.26 A in the AZSPWM3 to 1.16 A of the GTSPWM method for $M_i = 0.2$, and that is reduced from 6.34 A in AZSPWM3 to 5.44 A of the GTSPWM method for $M_i = 0.8$.

Fig. 26 shows the maximum harmonic magnitude around the first $f_{\rm s}$ for different PWM methods. The results are calculated by the powergui fast Fourier transformation analysis tool in MATLAB. The first $f_{\rm s}$ harmonic component of GTSPWM is

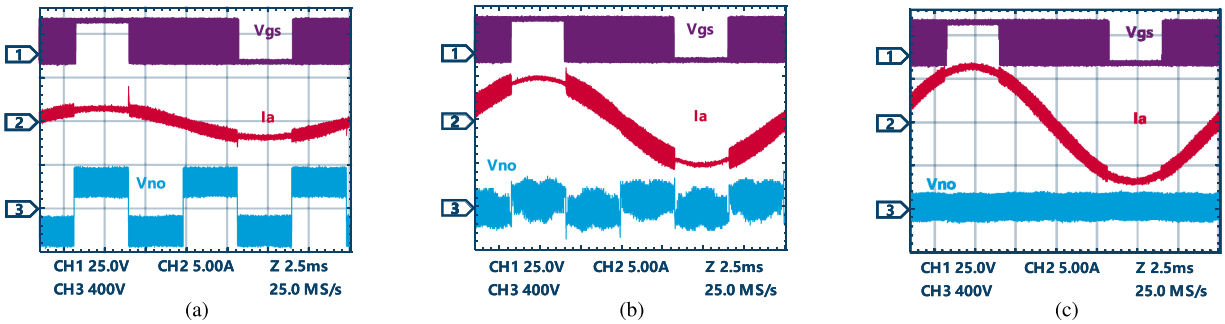

Fig. 22. Experimental waveforms of gate signal $V_{\rm gs}$, $I_{\rm a}$, and $V_{\rm no}$ for GTSPWM. (a) $M_i = 0.2$. (b) $M_i = 0.6$. (c) $M_i = 0.8$.

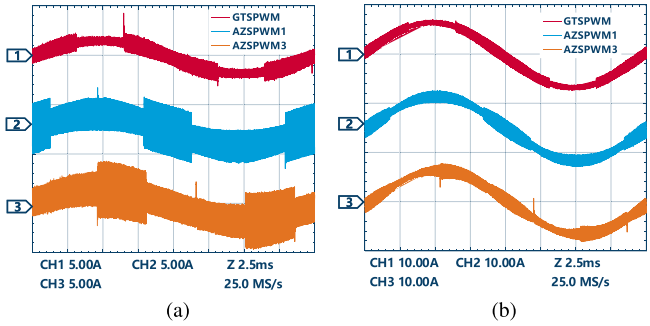

Fig. 23. Experimental waveforms of output phase current for different RCMV-PWM. (a) $M_i = 0.2$. (b) $M_i = 0.8$.

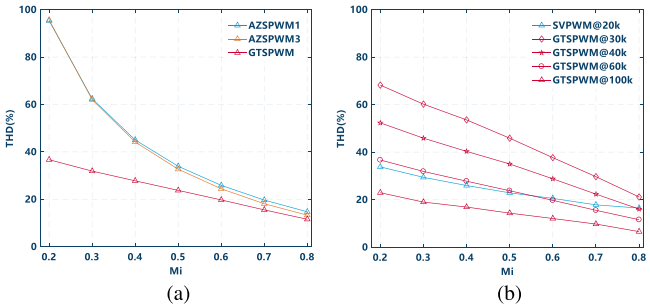

Fig. 24. THD comparison. (a) GTSPWM, AZSPWM1, and AZSPWM3. (b) GTSPWM and SVPWM.

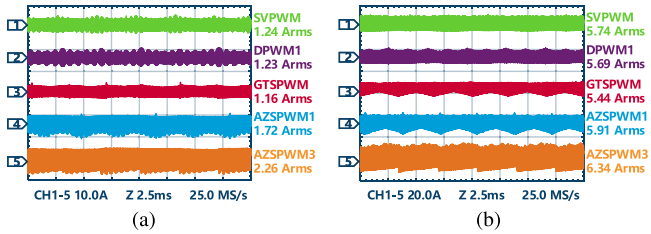

Fig. 25. DC-link current. (a) $M_i = 0.2$. (b) $M_i = 0.8$.

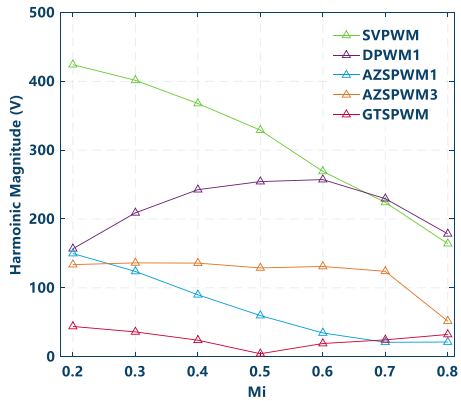

Fig. 26. Maximum harmonic magnitude around the first $f_{\rm s}$ for different PWM methods.

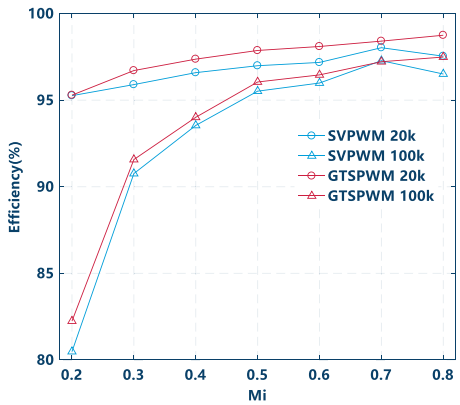

Fig. 27. Efficiency comparison between SVPWM and GTSPWM for different M_i.

lower than others as predicted with the normalized harmonic magnitude curve in Fig. 15(b).

Fig. 27 shows the efficiency comparison between SVPWM method and GTSPWM method. The efficiency is measured by Voltech PM6000 power analyzer. In the case of the SVPWM, the efficiency is lower than that with GTSPWM under the same switching frequency. When switching frequency increases from 20 to 100 kHz, the maximum efficiency of VSI using SVPWM method is decreased from 98.03% to 97.28%, while that of VSI with GTSPWM method is decreased from 98.75% to 97.49%. Therefore, with the usage of GTSPWM method, the switching frequency of SiC inverters can be further increased and the performance of high-frequency SiC inverters will be improved appreciably.

VII. Conclusion

This paper has proposed a novel GTSPWM method for high-frequency three-phase SiC VSIs with CMV reduction and improved performance. The working principles, switching signals, and drawbacks of conventional space vector based RCMV-PWM techniques have been reviewed. The proposed GTSPWM has been described and illustrated through generalized scalar PWM approach. The characteristics of GTSPWM have been investigated and compared with other well-studied RCMV-PWM methods. Both simulation and experiment results have been used to verify that GTSPWM-based high-frequency SiC VSIs achieve minimum switching losses, lesser current THD, smaller dc-link current ripples, and RCMV.

References

[1] Z. Zhang, F. Wang, L. M. Tolbert, B. J. Blalock, and D. J. Costinett, "Evaluation of switching performance of SiC devices in PWM inverter-fed induction motor drives," *IEEE Trans. Power Electron.*, vol. 30, no. 10, pp. 5701–5711, Oct. 2015.

[2] S. Hazra, S. Madhusoodhanan, G. K. Moghaddam, K. Hatua, and S. Bhattacharya, "Design considerations and performance evaluation of 1200-V 100-A SiC MOSFET-based two-level voltage source converter," *IEEE Trans. Ind. Appl.*, vol. 52, no. 5, pp. 4257–4268, Sep. 2016.

[3] Y. Liu *et al.*, "LCL filter design of a 50-kW 60-kHz SiC inverter with size and thermal considerations for aerospace applications," *IEEE Trans. Ind. Electron.*, vol. 64, no. 10, pp. 8321–8333, Oct. 2017.

[4] S. Yin, K. J. Tseng, C. F. Tong, R. Simanjorang, C. J. Gajanayake, and A. K. Gupta, "A 99% efficiency SiC three-phase inverter using synchronous rectification," in *Proc. IEEE Appl. Power Electron. Conf.*, Mar. 2016, pp. 2942–2949.

[5] K. Ali, R. K. Surapaneni, P. Das, and S. K. Panda, "A SiC MOSFET based nine-switch single-stage three-phase AC-DC isolated converter," *IEEE Trans. Ind. Electron.*, vol. 64, no. 11, pp. 9083–9093, Nov. 2017.

[6] N. Oswald, P. Anthony, N. McNeill, and B. H. Stark, "An experimental investigation of the tradeoff between switching losses and EMI generation with hard-switched All-Si, Si-SiC, and All-SiC device combinations," *IEEE Trans. Power Electron.*, vol. 29, no. 5, pp. 2393–2407, May 2014.

[7] C. Chen, Y. Chen, Y. Li, Z. Huang, T. Liu, and Y. Kang, "An SiC-based half-bridge module with an improved hybrid packaging method for high power density applications," *IEEE Trans. Ind. Electron.*, vol. 64, no. 11, pp. 8980–8991, Nov. 2017.

[8] C. C. Hou, C. C. Shih, P. T. Cheng, and A. M. Hava, "Common-mode voltage reduction pulsewidth modulation techniques for three-phase grid-connected converters," *IEEE Trans. Power Electron.*, vol. 28, no. 4, pp. 1971–1979, Apr. 2013.

[9] H. Chen and H. Zhao, "Review on pulse-width modulation strategies for common-mode voltage reduction in three-phase voltage-source inverters," *IET Power Electron.*, vol. 9, no. 14, pp. 2611–2620, Nov. 2016.

[10] M. H. Hedayati, A. B. Acharya, and V. John, "Common-mode filter design for PWM rectifier-based motor drives," *IEEE Trans. Power Electron.*, vol. 28, no. 11, pp. 5364–5371, Nov. 2013.

[11] W. Tan, C. Cuellar, X. Margueron, and N. Idir, "A high frequency equivalent circuit and parameter extraction procedure for common mode choke in the EMI filter," *IEEE Trans. Power Electron.*, vol. 28, no. 3, pp. 1157–1166, Mar. 2013.

[12] P. Garg, S. Essakiappan, H. S. Krishnamoorthy, and P. N. Enjeti, "A fault-tolerant three-phase adjustable speed drive topology with active common-mode voltage suppression," *IEEE Trans. Power Electron.*, vol. 30, no. 5, pp. 2828–2839, May 2015.

[13] A. M. Hava and E. Ün, "Performance analysis of reduced common-mode voltage PWM methods and comparison with standard PWM methods for three-phase voltage-source inverters," *IEEE Trans. Power Electron.*, vol. 24, no. 1, pp. 241–252, Jan. 2009.

[14] E. Un and A. M. Hava, "A near-state PWM method with reduced switching losses and reduced common-mode voltage for three-phase voltage source inverters," *IEEE Trans. Ind. Appl.*, vol. 45, no. 2, pp. 782–793, Mar. 2009.

[15] A. M. Hava and E. Ün, "A high-performance PWM algorithm for common-mode voltage reduction in three-phase voltage source inverters," *IEEE Trans. Power Electron.*, vol. 26, no. 7, pp. 1998–2008, Jul. 2011.

[16] H. Lu, W. Qu, X. Cheng, Y. Fan, and X. Zhang, "A novel PWM technique with two-phase modulation," *IEEE Trans. Power Electron.*, vol. 22, no. 6, pp. 2403–2409, Nov. 2007.

[17] H. Lu, X. Cheng, W. Qu, S. Sheng, Y. Li, and Z. Wang, "A three-phase current reconstruction technique using single DC current sensor based on TSPWM," *IEEE Trans. Power Electron.*, vol. 29, no. 3, pp. 1542–1550, Mar. 2014.

[18] J. W. Kimball and M. Zawodniok, "Reducing common-mode voltage in three-phase sine-triangle PWM with interleaved carriers," *IEEE Trans. Power Electron.*, vol. 26, no. 8, pp. 2229–2236, Aug. 2011.

[19] J. Huang and H. Shi, "Suppressing low-frequency components of commonmode voltage through reverse injection in three-phase inverter," *IET Power Electron.*, vol. 7, no. 6, pp. 1644–1653, Jun. 2014.

[20] X. Wu, G. Tan, Z. Ye, Y. Liu, and S. Xu, "Optimized common-mode voltage reduction PWM for three-phase voltage-source inverters," *IEEE Trans. Power Electron.*, vol. 31, no. 4, pp. 2959–2969, Apr. 2016.

[21] S. Kwak and S. K. Mun, "Model predictive control methods to reduce common-mode voltage for three-phase voltage source inverters," *IEEE Trans. Power Electron.*, vol. 30, no. 9, pp. 5019–5035, Sep. 2015.

[22] A. M. Hava, R. J. Kerkman, and T. A. Lipo, "Simple analytical and graphical methods for carrier-based PWM-VSI drives," *IEEE Trans. Power Electron.*, vol. 14, no. 1, pp. 49–61, Jan. 1999.

[23] A. M. Hava, R. J. Kerkman, and T. A. Lipo, "A high-performance generalized discontinuous PWM algorithm," *IEEE Trans. Ind. Appl.*, vol. 34, no. 5, pp. 1059–1071, Sep. 1998.

[24] O. Ojo, "The generalized discontinuous PWM scheme for three-phase voltage source inverters," *IEEE Trans. Ind. Electron.*, vol. 51, no. 6, pp. 1280–1289, Dec. 2004.

[25] T. D. Nguyen, J. Hobraiche, N. Patin, G. Friedrich, and J. P. Vilain, "A direct digital technique implementation of general discontinuous pulse width modulation strategy," *IEEE Trans. Ind. Electron.*, vol. 58, no. 9, pp. 4445–4454, Sep. 2011.

[26] S. L. An, X. D. Sun, Q. Zhang, Y. R. Zhong, and B. Y. Ren, "Study on the novel generalized discontinuous SVPWM strategies for three-phase voltage source inverters," *IEEE Trans. Ind. Informat.*, vol. 9, no. 2, pp. 781–789, May 2013.

[27] A. M. Hava and N. O. Çetin, "A generalized scalar PWM approach with easy implementation features for three-phase, three-wire voltage-source inverters," *IEEE Trans. Power Electron.*, vol. 26, no. 5, pp. 1385–1395, May 2011.

[28] J. W. Kolar and S. D. Round, "Analytical calculation of the RMS current stress on the DC-link capacitor of voltage-PWM converter systems," *IEE Proc.—Electric Power Appl.*, vol. 153, no. 4, pp. 535–543, Jul. 2006.

[29] J. W. Kolar, H. Ertl, and F. C. Zach, "Influence of the modulation method on the conduction and switching losses of a PWM converter system," *IEEE Trans. Ind. Appl.*, vol. 27, no. 6, pp. 1063–1075, Nov. 1991.

[30] D. G. Holmes and T. A. Lipo, *Modulation of Three Phase Voltage Source Inverters*. New York, NY, USA: Wiley-IEEE Press, 2003, pp. 215–258. [Online]. Available: http://ieeexplore.ieee.org/xpl/articleDetails.jsp?arnumber=5311949

Junzhong Xu (S'17) was born in Ningbo, China, in 1994. He received the B.S. degree in electrical engineering from Harbin Institute of Technology, Harbin, China, in 2016. He is currently working toward the Ph.D. degree in electrical engineering with the Department of Electrical Engineering, Shanghai Jiao Tong University, Shanghai, China.

His research interests include wide band gap (SiC and GaN) power device applications, motor drive inverts, and grid-tied inverter.

Jingwen Han was born in Shuozhou, China, in 1996. She is currrently a Senior Student in electrical engineering with the Department of Electrical Engineering, Shanghai Jiao Tong University, Shanghai, China.

Her research interests include wide band gap (SiC and GaN) power device applications and grid-tied inverter.

Yong Wang (M'12) received the Ph.D. degree in power electronics from Zhejiang University, Hangzhou, China, in 2005.

After receiving the Ph.D. degree, from 2005 to 2008, he was a Senior Researcher with Samsung Advanced Institute of Technology, Suwon, South Korea, researching on the fuel cell grid-tied inverter. From 2008 to 2010, he was working with Danfoss, Soenderborg, Denmark, as a power electronics Hardware Engineer. In the year 2010, he joined Shanghai Jiao Tong University, Shanghai, China, where he is currently a Full Professor with the Department of Electrical Engineering. His main research interests include active power filter, multilevel conversion technology, SiC inverter, grid-tied inverter, LLC, and so on.

Muhammad Ali was born in Peshawar, Pakistan, in 1991. He received the Engineer's and M.S. degrees in electrical engineering from the Sarhad University of Science and Technology, Peshawar, Pakistan, in 2013 and 2015, respectively. He is currently working toward the Ph.D. degree in electrical engineering with Shanghai Jiao Tong University, Shanghai, China.

His research interests includes power converters, smart grid, and renewable energy systems.

Houjun Tang received the Ph.D. degree from Yamagata University, Yamagata, Japan, in 1997.

He is currently a Full Professor with the Department of Electrical Engineering, Shanghai Jiao Tong University, Shanghai, China. His research interests include wireless power transform, motor drive inverters, and power conversion.